Journal of
MATERIALS RESEARCH

A transmission electron microscopy investigation of sulfide nanocrystals formed by ion implantation

A. Meldrum,[a] E. Sonder, R.A. Zuhr, I.M. Anderson, J.D. Budai, C.W. White, and L.A. Boatner
Oak Ridge National Laboratory, Oak Ridge, Tennessee 37831

D.O. Henderson
Fisk University, Department of Physics, Nashville, Tennessee 37208

(Received 23 February 1999; accepted 3 September 1999)

Ion implantation was used to form compound semiconductor nanocrystal precipitates of ZnS, CdS, and PbS in both glass and crystalline matrices. The precipitate microstructures and size distributions were investigated by cross-sectional transmission electron microscopy techniques. Several unusual features were observed, including strongly depth-dependent size variations of the ZnS precipitates and central void features in the CdS nanocrystals. The morphology and crystal structure of the nanocrystal precipitates could be controlled by selection of the host material. The size distribution and microstructural complexity were significantly reduced by implanting a low concentration of ions into a noncrystalline host, and by using multi-energy implants to give a flat concentration profile of the implanted elements.

I. INTRODUCTION

The electronic and optical properties of semiconductors in the form of nanometer-scale precipitates are strongly particle size dependent. The band gap can, in fact, be tuned by controlling the size of the semiconductor nanocrystals.[1,2] This tunability is due to a localization of carrier wave functions (i.e., quantum confinement). Quantum confinement occurs when the diameter of the nanocrystal is less than the exciton Bohr radius. This localization causes an increase in the effective band gap that can be measured by a shift of the optical absorption edge to higher energies. The absorption spectrum can, therefore, be tailored by controlling the particle size.[1] In the transition-metal chalcogenides (e.g., CdS, PbS, CdSe), the observed shifts in the optical absorption spectrum may represent a large portion of the band gap. Strong size-dependent photoluminescence may also be observed in the visible and near-infrared portions of the spectrum (e.g., see Ref. 3) and the origin of this luminescence may be strongly affected by surface states.[4]

A number of studies of the optoelectronic properties of sulfide nanocrystals have recently been conducted,[5–10] and several synthesis techniques were developed.[7,9–14] For optical device applications (e.g., optical switches, all-optical memory, solar cells), the synthesis technique should produce a large volume-filling fraction of nanocrystals in a transparent and durable host. Additionally, a narrow particle size distribution is generally desirable to resolve the fine structure arising from quantum-confinement effects. A flexible synthesis technique should be easily applicable to a variety of optical host materials, should provide experimental control over the volume fraction of nanocrystals, and should, if necessary, provide a suitably narrow size distribution of precipitates. The narrowest size distributions have thus far been obtained by wet chemical synthesis techniques (e.g., see Refs. 15 and 16); however, to date this technique has not produced nanocrystals embedded in a solid matrix suitable for the device applications noted above.

Ion-implantation has been established as a practical technique for fabricating sulfide nanocrystals.[17–19] The elements forming the compound are implanted sequentially into a selected matrix, thereby producing a supersaturated solid solution in the implanted region. Thermal processing at elevated temperatures then results in the nucleation and growth of the compound nanocrystal precipitates. Ion implantation is flexible in that nanocrystals can be synthesized in almost any host material in which the implanted constituents are relatively insoluble or have a high free energy of formation, and the average size and microstructure of the precipitates can be controlled by varying the implantation and annealing parameters.[20,21] The main disadvantage of ion implantation is that a relatively wide size distribution of nanocrystals is usually produced—a problem that currently limits the utilization of this technique for device applications.

[a]Present address: The University of Alberta, Department of Physics, Edmonton, Alberta, Canada T6G 2J1.

In this work, transmission electron microscopy (TEM) is used to carry out a systematic study of the microstructure and size distribution of compound semiconductor nanocrystals as a function of dose, implant temperature, implant order, annealing conditions (temperature and atmosphere), and host composition. The two primary objectives of this work are to characterize the often unusual microstructures of sulfide nanocrystals formed in various host materials and to suggest avenues by which narrower size distributions and simpler microstructures may be obtained.

II. EXPERIMENTAL

High-purity fused SiO_2 glass (Corning 7940), *c*-axis-oriented single-crystal α–Al_2O_3, and [001]-oriented Si wafers were used as host materials. TRIM-96[22] calculations were used to determine the appropriate ion energies to produce overlapping concentration profiles of the implanted ions. The samples were clipped onto a steel backing plate and, unless specified otherwise, were implanted at room temperature using a beam current density of approximately 4 $\mu A/cm^2$. The maximum temperature increase during implantation of these samples was estimated with basic heat flow equations to be approximately 200 °C. Other samples were heat sunk and cooled to liquid nitrogen temperature during implantation. Several specimens were also implanted using a range of ion energies to give a near-uniform concentration (flat profile) of the implanted species. The crystalline α–Al_2O_3 and Si host materials were implanted at elevated temperature to prevent beam-induced amorphization. In most cases, the cation (Zn, Cd, or Pb) was implanted first. The samples were annealed in a flowing 96% Ar + 4% H_2 atmosphere. Some anneals were repeated with argon only, and some samples were not annealed. A complete list of the implant and annealing conditions for the samples in the present study is given in Table I.

Sample characterization was done by Rutherford backscattering spectroscopy with 2.3 MeV He^{2+} ions and a detector angle of 160°. X-ray diffraction measurements with a four-circle Huber diffractometer and Cu K_α x-rays were used to identify the precipitated compounds. Cross-sectional TEM samples were prepared by gluing the implanted specimen to a silicon wafer and hand-polishing to a thickness of about 1 μm. This thickness estimate is based on the color of the silicon wafer in transmitted light.[23] The specimens were then ion-milled for 15 to 45 min at liquid nitrogen temperature with 4-keV Ar^+ ions with a beam current of 1 mA and an incident angle of 12°. This technique generally provides extensive thin areas containing the implanted elements. The specimens were examined in a Philips EM400 TEM operated at 100 kV and in a Philips CM200 FEG STEM operated at 200 kV. The chemical composition of the implanted region was obtained by energy dispersive x-ray spectrometry (EDS) with a thin-window detector and EmiSPEC data acquisition and analysis software. Parallel electron energy loss spectrometry (PEELS) was performed on a Philips CM30 TEM equipped with a Gatan imaging filter.

TABLE I. Implant and annealing conditions for the specimens shown in Figs. 1–10. The average diameter and standard deviation (a measure of the size distribution) of the sulfide nanocrystals are given in the final two columns. These values were not obtained for Al_2O_3–PbS and Al_2O_3–ZnS because many of the nanocrystals coalesced to form a semicontinuous layer. For the multienergy-implanted specimens, ion energies were chosen to give a relatively flat concentration profile over a range of at least 100 nm

	Implant conditions				Annealing conditions			Measurements	
Specimen	Cation energy (keV)	Anion energy (keV)	Dose ions/cm^2	Temperature (°C)	Atmosphere	Time (min)	Temperature (K)	Average size (nm)	Standard deviation
SiO_2–ZnS–1	multi		1.7×10^{16}	25	Ar + 4%H_2	60	1000	2.4	0.4
SiO_2–ZnS–2	multi		1.4×10^{17}	25	Ar + 4%H_2	60	1000	7.5	5.3
SiO_2–ZnS–3	multi		1.4×10^{17}	25	Ar + 4%H_2	60	1000	7.8	6.1
SiO_2–ZnS–4	320	180	1.0×10^{17}	25	not annealed			5.6	2.3
SiO_2–ZnS–5	320	180	1.0×10^{17}	25	Ar + 4%H_2	6	1000	6.5	3.9
SiO_2–ZnS–6	320	180	1.0×10^{17}	25	Ar	60	1000	8.2	6.0
SiO_2–CdS–1	multi		1.0×10^{16}	25	Ar + 4%H_2	60	1000	4.9	1.3
SiO_2–CdS–2	multi		2.8×10^{16}	25	Ar + 4%H_2	60	1000	6.5	2.2
SiO_2–CdS–3	multi		7.5×10^{16}	25	Ar + 4%H_2	60	1000	9.8	3.6
SiO_2–PbS–1	320	82	2.5×10^{16}	25	Ar + 4%H_2	60	1000	6.8	3.4
SiO_2–PbS–2	320	82	7.5×10^{16}	25	Ar + 4%H_2	60	1000	8.5	9.5
SiO_2–CdSe	450	330	1.0×10^{17}	25	Ar + 4%H_2	60	1000	10.5	8.4
Al_2O_3–ZnS	280	150	6.0×10^{16}	700	Ar + 4%H_2	60	1000	not obtained	
Al_2O_3–CdS	450	164	4.3×10^{16}	900	Ar + 4%H_2	60	1000	17.7	12.4
Al_2O_3–PbS	850	180	5.0×10^{16}	850	Ar + 4%H_2	60	1000	not obtained	
Si–ZnS	280	160	5.0×10^{16}	823	Ar + 4%H_2	60	1000	14.0	7.9
Si–CdS	410	150	3.0×10^{16}	823	Ar + 4%H_2	60	1000	13.7	8.5

III. RESULTS

A. Sulfide nanocrystals in SiO_2 glass

1. ZnS nanocrystals

The TEM results for the multienergy, flat profile implants (specimens SiO_2–ZnS–1 and SiO_2–ZnS–2) are shown in Fig. 1 (a) and (b). For the lowest-concentration specimen (1.7×10^{16} ions/cm^2, corresponding to a maximum implanted concentration of 0.5×10^{21} ions/cm^3 in the flat profile region as determined by Rutherford backscattering spectrometry (RBS) measurements: sample SiO_2–ZnS–1), cross-sectional TEM and electron diffraction revealed the presence of a layer of randomly oriented, spherical, wurtzite-structure nanocrystals extending from the surface to a depth of 300 nm in the fused silica. The precipitates are approximately 2.5 nm in diameter on average (Table I). A few isolated, relatively large (about 6 nm in diameter) nanocrystals occur near the calculated maximum depth of the ion damage [about 300 nm: see Fig. 1(a)]. With the exception of these isolated larger precipitates, the size dispersion is relatively narrow in this specimen (standard deviation = 0.4 nm).

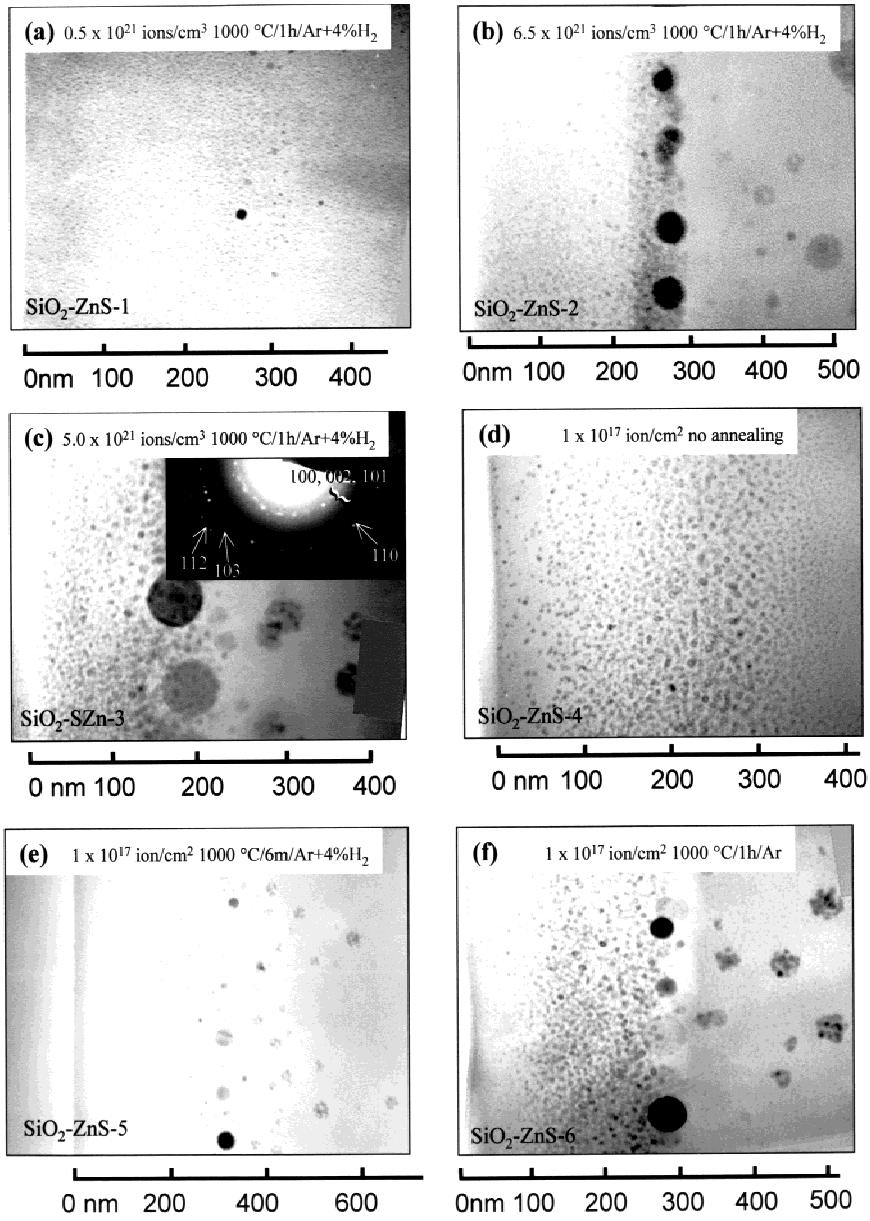

FIG. 1. ZnS precipitates in silica glass. All specimens were implanted at room temperature (not heat sunk). The implanted concentration [(a), (b), and (c) flat profile implants] or dose [(d), (e), and (f) single-energy implants] and the annealing conditions (temperature/time/atmosphere) are indicated at the top of each micrograph. The specimen number (corresponding to Table I) is indicated in the bottom left. (c) A representative electron-diffraction pattern is given and is indexed to the wurtzite phase of ZnS.

At a higher implant dose (1.4×10^{17} ions/cm^2, or 6.5×10^{21} ions/cm^3; multienergy sample SiO_2–ZnS–2), the size distribution is distinctly bimodal [Fig. 1(b)]. A layer of large ZnS nanocrystals formed near the calculated end-of-range of the highest-energy implanted ions. The average diameter of these larger precipitates is about 30 nm. RBS results showed a corresponding increase in the implanted zinc concentration at a depth corresponding to the location of the larger precipitates. In contrast, the ZnS precipitates nearer the surface are only 6 nm in diameter on average. Electron diffraction confirmed the wurtzite structure for the annealed SiO_2–ZnS specimens (Fig. 1), but a minor zincblende component was detected by x-ray diffraction. At depths between 300 and 1000 nm (beyond the implanted region), structures with a spherulitic "snowflake" shape are dispersed in the glassy matrix. These structures were observed in every thermally processed SiO_2–ZnS specimen in these experiments. Electron-diffraction patterns from these features were consistent with the γ phase of Zn_2SiO_4.

The effect of the implant order on the bimodal size distribution was investigated by fabricating an additional flat-profile sample, but this time with the sulfur implanted before the zinc. As with the previous specimens, a bimodal distribution of precipitates formed [Fig. 1(c)], but the layer of larger precipitates occurred at a shallower depth and the spherulites of γ–Zn_2SiO_4 beyond this layer were more numerous than in the specimens implanted with zinc first.

The development of the bimodal size distribution was investigated by examining additional samples before and after a short duration anneal. A specimen was prepared with only a single ion energy for each implanted species (320 keV Zn + 180 keV S, dose = 1×10^{17} ions/cm^2). The sample was not heat sunk during implantation. After implantation, the sample was broken into three pieces. One piece was not annealed [Fig. 1(d)], another was annealed for 6 min at 1000 °C in Ar + 4%H_2 [Fig. 1(e)], and the third was annealed for 1 h in an Ar atmosphere [Fig. 1(f)]. Figure 1(d) shows that ZnS precipitates actually formed during the implantation (confirmed by electron diffraction) and that the size distribution is unimodal. After annealing for only 6 min, a layer of larger precipitates develops at a depth of about 300 nm. After annealing for 1 h in an Ar-only atmosphere, the layer is well developed and the precipitates in the layer are as large as 100 nm in diameter. In general, the size distribution of ZnS nanocrystals in the specimens implanted with a single ion energy was slightly larger than for the flat-profile specimens (Table I).

To further investigate this unusual microstructure, additional samples were implanted with zinc only or with sulfur only (single ion energy) and were then annealed at temperatures of 800 to 1000 °C. In the Zn-implanted specimens annealed at 800 °C, the resulting size distribution of Zn precipitates is clearly bimodal, with two layers of larger Zn colloids at depths of about 110 and 210–250 nm, respectively (Fig. 2). These layers correspond closely to the region of maximum implanted Zn concentration and the maximum depth of the ion-irradiation damage, as calculated by TRIM-96. The larg-

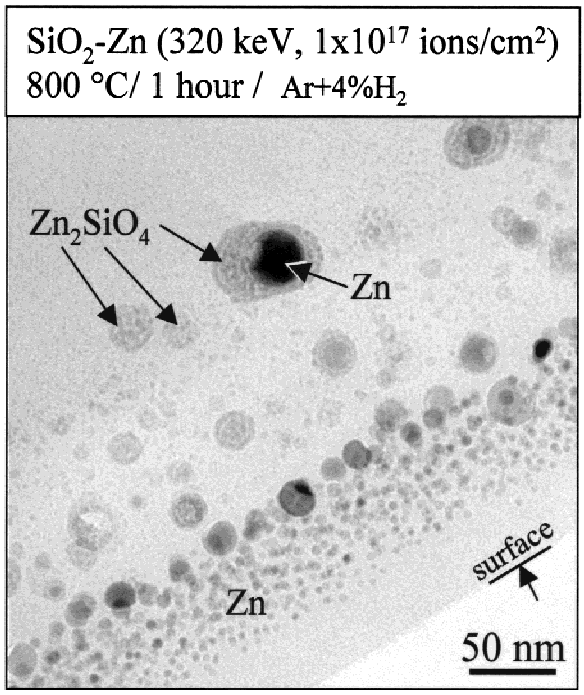

(a)

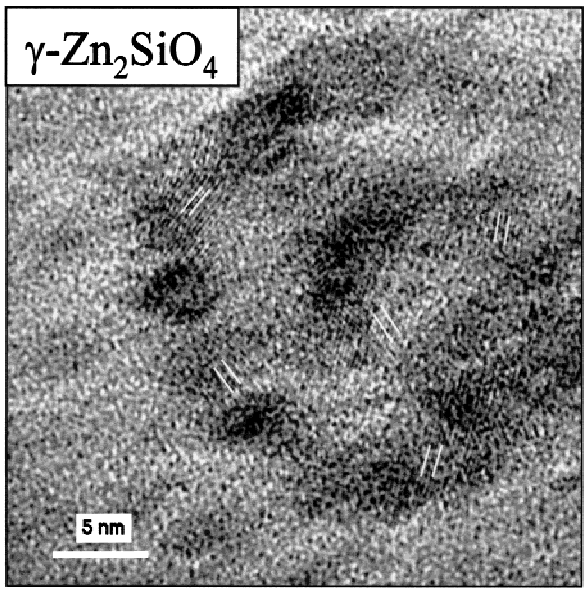

(b)

FIG. 2. Cross-sectional (a) and high-resolution (b) micrographs of silica glass implanted with Zn only and annealed at 800 °C for 1 h. The overall microstructure is similar to that for the SiO_2–ZnS specimens, with small particles nearer the surface and a layer of large precipitates and the calculated boundary between the ion-beam-damaged SiO_2 at the nonirradiated SiO_2 at deeper levels. Spherulites of Zn_2SiO_4 encapsulating large metallic Zn precipitates are located at a depth of ~300 nm.

est Zn colloids are invariably embedded within an aggregate of light-contrast polycrystalline material (see Fig. 2). After annealing at 1000 °C, however, Zn-implanted SiO_2 specimens contained polycrystalline spherules, morphologically similar to those located at depths greater than 300 nm in the Zn + S-implanted samples described above, but no Zn precipitates. Convergent beam electron diffraction techniques were used to identify the spherules as aggregates of γ-Zn_2SiO_4. In contrast, a layer of bubbles was observed in the specimens implanted with sulfur only. The bubbles were located at a depth of about 150 nm, and they disappeared after a short duration exposure in the electron beam. No crystalline particles were observed, and no unusual microstructures were present at the depth where the larger precipitates formed in the Zn-implanted specimen.

An additional experiment was performed to determine whether the ZnS particle size distribution could be narrowed by nonthermal nucleation and growth of the particles. A specimen of SiO_2 was implanted to a dose of 1×10^{17} ions/cm^2 of Zn and S. In this case, the specimen was heat sunk to minimize specimen heating during implantation and thereby prevent the nucleation of particles. A cross-sectional TEM specimen was prepared and the implanted layer was irradiated with a moderately defocused electron beam directly in the TEM (beam current = 1 nA, current density = 1 A/cm^2). In the as-implanted state, ZnS nanocrystalline precipitates are not present in the implanted layer (Fig. 3a). However, after a few minutes of electron irradiation in the TEM, areas of dark contrast were observed in the TEM micrographs. After approximately 10 min of irradiation, no further microstructural evolution occurred and the sample then consisted of randomly oriented ZnS nanocrystals [Fig. 3(c)]. The size distribution of the particles is narrow [average diameter = 3.1 nm, standard deviation = 0.45 nm; Fig. 3(d)], suggesting that this technique may be useful in forming monodispersed particles of ZnS. Electron energies as low as 60 or 100 keV were also sufficient to nucleate ZnS precipitates from the same specimen.

2. CdS nanocrystals

TEM images for the three SiO_2–CdS flat-profile specimens are shown in Fig. 4. Electron- and x-ray diffraction results showed that wurtzite-structure CdS nanocrystals formed in silica glass, and the precipitate composition was confirmed by EDS analysis. The average size and size distribution of the precipitates decrease with decreasing dose (Table I, Fig. 4). At the lowest implanted dose (1.0×10^{16} ions/cm^2, or 0.8×10^{21} ions/cm^3 in the flat profile region) the nanocrystals appear as rather poorly defined dark regions with an average diameter of less than 5 nm. The average size increases to approximately 6.5 and 9.8 nm in diameter for implant doses of 2.8×10^{16} and 7.5×10^{16} ions/cm^2, respectively (corresponding to concentrations of 2.0×10^{21} ions/cm^3 and 5.3×10^{21} ions/cm^3). The standard deviations are proportionally higher as the concentration increases. The size distribution is unimodal, in contrast to the bimodal distribution observed for the annealed ZnS precipitates. In the three flat-profile specimens, the average size of the precipitates is constant between depths of about 50 and 160 nm. RBS measurements showed that the implanted concentration of Cd and S were nearly uniform in this depth range.

Many of the CdS precipitates in specimen SiO_2–CdS–3 (the highest dose implant) typically appear to be ring shaped with an area of light contrast in the central region [Fig. 4(c)]. This feature is especially striking in the largest precipitates. The lattice fringes continue uniformly through the center of the crystallites (Fig. 5). Tilting the specimen did not reverse the contrast across these features; i.e., the central region always showed the lightest contrast.

Energy-filtered imaging was used to investigate the nature of these light-contrast features. The sample was ion-milled so that the largest nanocrystals were present in areas suitably thin for electron energy loss spectrometry (EELS), where plural scattering is negligible. Zero-loss and low-loss images were acquired from a region of the

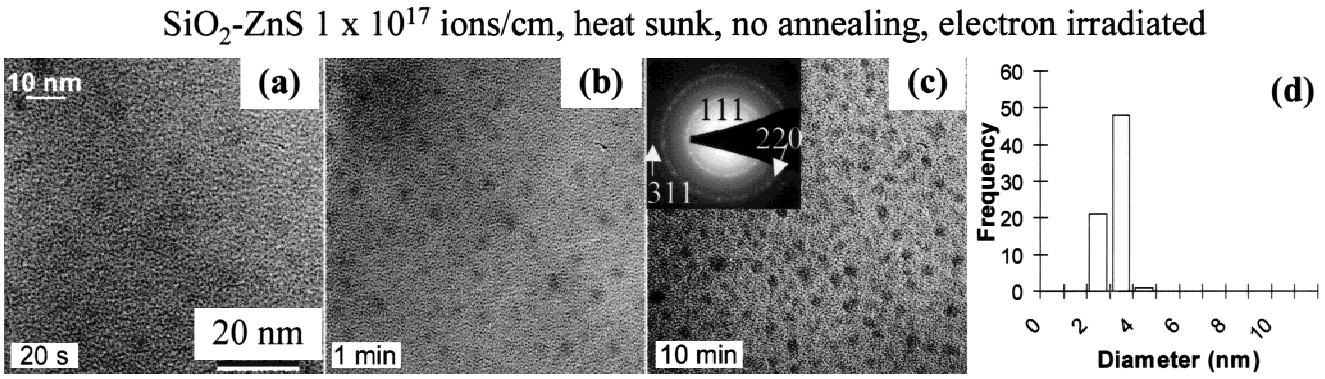

FIG. 3. (a–d) Electron-irradiation-induced precipitation of monodispersed zincblende-structure ZnS nanocrystals in silica glass. The specimen was heat sunk during ion implantation to prevent the growth of particles. The electron beam current was 1 nA (current density ≅ 1 A/cm^2).

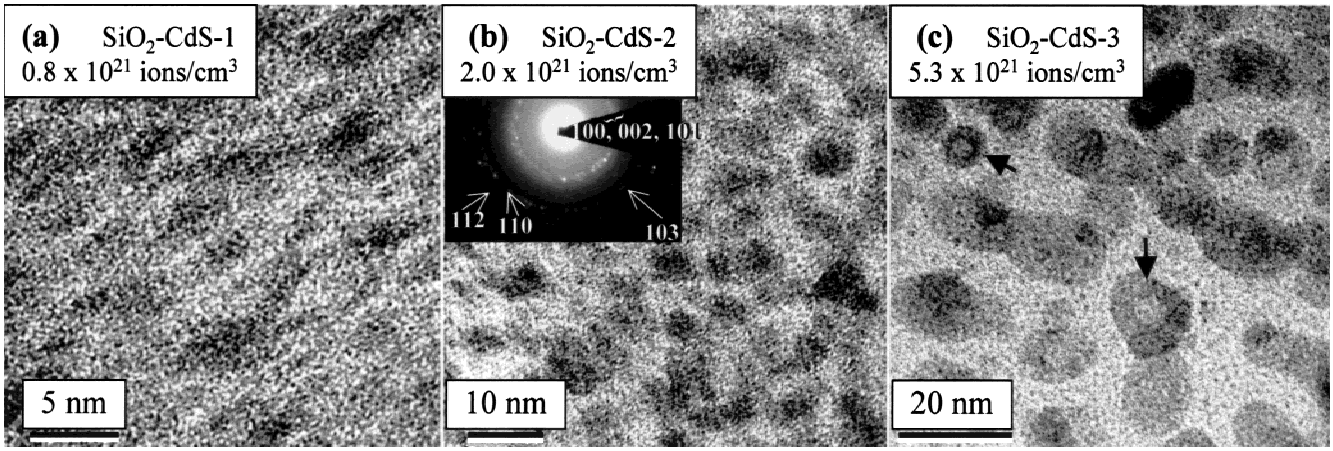

FIG. 4. (a) CdS precipitates in silica glass. All three flat-profile specimens were annealed for 1 h in flowing Ar + 4%H_2 (Table I). (b) A representative electron-diffraction pattern is given and is indexed to the wurtzite phase of CdS. (c) Arrows point to clear examples of ring-shaped nanoparticles. The implanted concentration in the flat profile region as measured by RBS is given at the top of each image. See Table I for the corresponding dose in units of ions/cm^2.

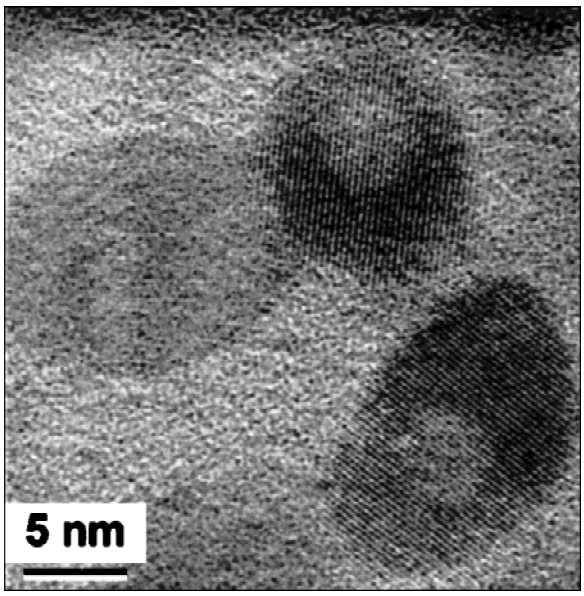

FIG. 5. High-resolution image of CdS precipitates. Note the light-contrast feature in the center of the particles.

specimen containing the ring-shaped nanoparticles by using a post-column Gatan imaging filter (GIF). The zero-loss image was formed by allowing only a narrow energy band of electrons centered about the zero-energy-loss position to form the image, so that the inelastically scattered plasmon-loss and core-loss electrons are excluded. The low-loss image is acquired with the slit removed, so that both zero-loss and inelastically scattered electrons are used to form the image. Such images are shown in Fig. 6. A measure of the local mass thickness is given by the relation

$$t/\lambda = \ln(I_L/I_0) \quad , \qquad (1)$$

where t is the thickness of the specimen, λ is the mean free path for inelastic scattering, and I_0 and I_L are the intensities in the zero-loss and low-loss images, respectively. Typically, the mean free path is smaller for materials of higher atomic number, and t/λ is, therefore, correspondingly higher for a constant specimen thickness. A t-over-λ map is shown in Fig. 6, as well as a profile of t/λ across the ring-shaped particle. The mass thickness is clearly higher when the beam passes through the side walls of the particle, but the mass thickness in the center of the particle is similar to the surrounding matrix. Given that at the center of the particle the beam probably passes through the ~5-nm-thick top and bottom surfaces of the higher-density particles, it follows that the core of the particles must be of a much smaller mass thickness than the edges. This can be accounted for only by the presence of significantly lower-density material in the central portion of the particles. The central regions are, therefore, probably either voids or bubbles. This identification is also consistent with the invariably light diffraction contrast from the precipitate cores.

3. PbS nanocrystals

Randomly-oriented PbS nanocrystals were formed by sequential ion implantation of Pb and S into SiO_2. TEM observations show a band of PbS precipitates from a depth of 10 to 180 nm, with the largest particles centered at a depth of ~90 nm (Fig. 7). The precipitates have the cubic rock salt structure and, for an implanted dose of 2.5×10^{16} ions/cm^2 (SiO_2–PbS–1), the largest nanocrystals are located at the calculated peak of the implanted concentration profile. For a dose of 7.5×10^{16} ions/cm^2, the precipitates at the center of the profile have a diameter approaching 100 nm. In the high-dose specimen, the size distribution is roughly bimodal, and the largest

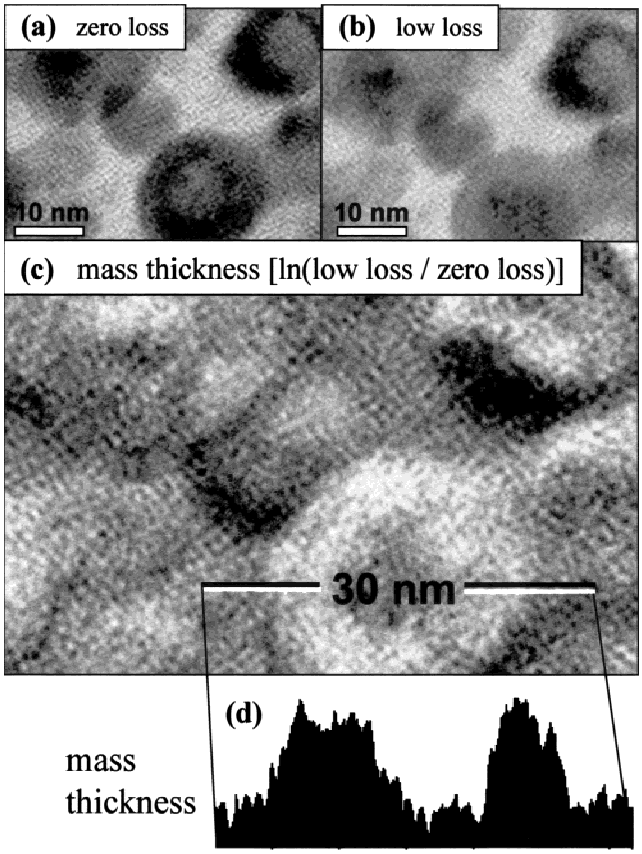

FIG. 6. EELS images of several CdS precipitates from sample SiO_2–CdS–3. Separate (a) zero-loss and (b) low-loss images were collected and were combined to produce (c) a mass thickness image (see text). The intensity in this image is related to the relative mass thickness of the sample. A mass profile across one of the CdS nanocrystals is shown in (d).

nanocrystals form at the calculated peak of the concentration profile. No central contrast features were observed in the larger nanocrystals, and no separate phases were identified.

4. CdSe nanocrystals

Solutions of well-formed CdSe nanocrystals and even three-dimensional superlattices of CdSe precipitates[24] have previously been synthesized by chemical techniques, and their microstructure and size distributions were extensively characterized.[25] CdSe nanocrystals can also be formed by ion implantation. In this work, we compare the microstructure of selenide nanocrystals to that of the analogous sulfide composition (i.e., CdS). The Cd and Se implant and annealing parameters are given in Table I, and the resulting microstructure is shown in Fig. 8. X-ray and electron diffraction confirmed that the precipitates are, indeed, hexagonal CdSe. Similar to the case of ZnS, the particle size distribution is distinctly bimodal. CdSe precipitates occurring in the first 150 nm from the surface average 6 nm in diameter. Ring-shaped

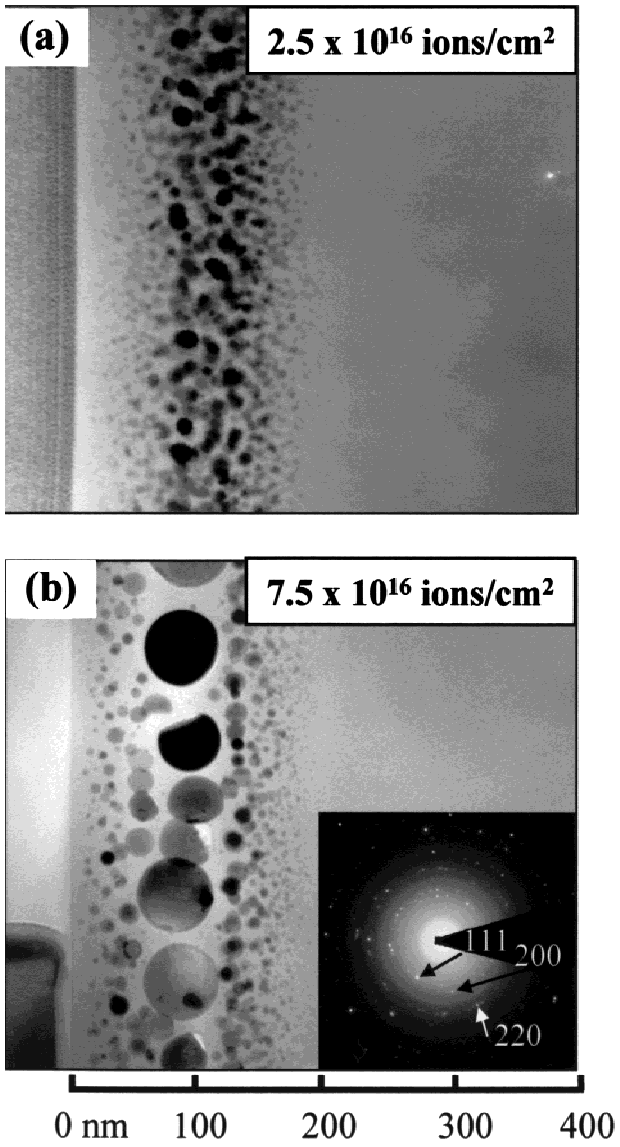

FIG. 7. (a,b) PbS precipitates in silica glass. Both specimens were annealed for 1 h in flowing Ar + 4%H_2 (Table I).

particles were also observed [Fig. 8(d)], although they were less common than in the case of CdS. The large precipitates are not, however, confined to a single layer as for ZnS, but instead they extend to depths up to approximately triple the calculated end-of-range of the implanted ions. High-resolution imaging of these large particles gives lattice spacings and symmetry that are consistent with hexagonal CdSe [Fig. 8(b)]. These structures were not identified in a previous study (Ref. 18) because the cross-sectional image was cut off at a depth of 150 nm.

B. Sulfide nanocrystals in Al_2O_3

Ion implantation was used to form ZnS, CdS, and PbS precipitates by implanting the constituent elements into *c*-axis-oriented α–Al_2O_3 hosts followed by thermal proc-

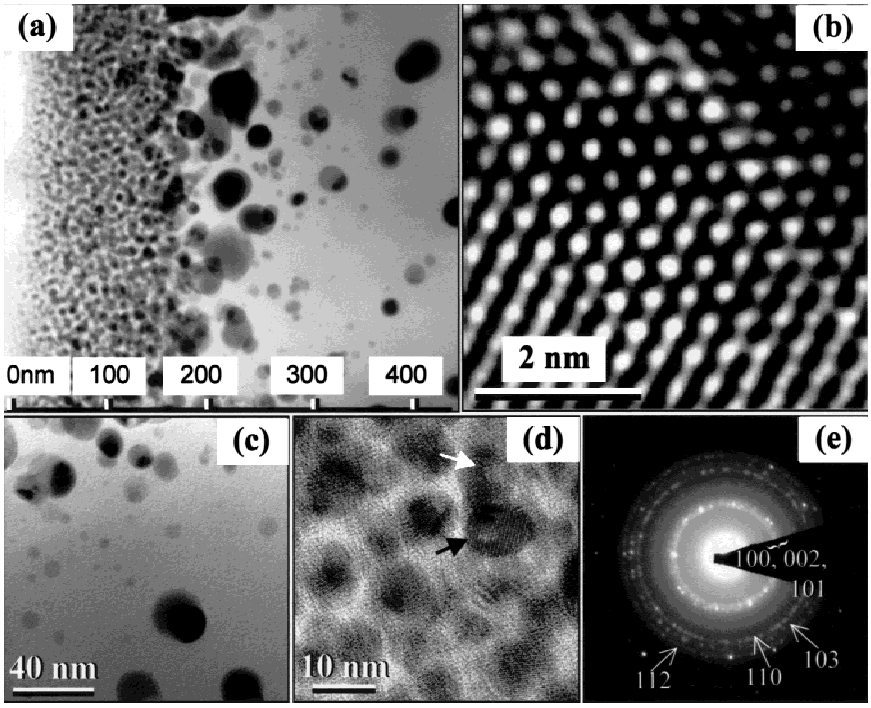

FIG. 8. CdSe precipitates in silica glass. (a) Cross-sectional view, (b) high-resolution image of one of the large particles from a depth of 200 nm, (c) distribution of precipitates at a depth of ~200 nm, (d) high-resolution image showing the distribution of particles at a depth of ~75 nm, (e) electron-diffraction pattern from the region imaged in (d). This diffraction pattern is indexed to hexagonal CdSe. In (a) and (c) darker regions are produced by overlapping particles, and in (d) arrows point to examples of particles with a central light-contrast feature.

essing. The implantation and annealing conditions were generally the same as for the SiO_2 glass substrates (Table I), except that the implantations were performed at elevated temperature to prevent beam-induced amorphization of the alumina. In all cases, the sulfide nanocrystals created by ion implantation into α–Al_2O_3 were faceted and crystallographically aligned with the Al_2O_3 lattice.

A θ-2θ x-ray scan in Fig. 9(a) (bottom) shows ZnS peaks, which can be indexed by using either the hexagonal wurtzite or the cubic zincblende structure. X-ray scans along additional crystallographic directions showed that there is actually a mixture of both phases with either the $[0001]_{\text{wurtzite}}$ or the $[111]_{\text{zincblende}}$ axis of the ZnS precipitates aligned parallel to the [0001] axis of the Al_2O_3 host. The size distribution of the ZnS nanocrystals is broad and in several regions the particles appear to have coagulated to form a semicontinuous layer [Fig. 9(a)].

CdS nanocrystals were also produced in an α–Al_2O_3 matrix [Fig. 9(b)]. All the peaks observed for CdS are indexable to the wurtzite structure, although the zincblende or rock salt phases could also be present in minor quantities. The implanted dose was lower than for the case of ZnS, and the precipitates did not coagulate into a semicontinuous layer, although the structure and orientation of the particles is the same as for the ZnS precipitates. The CdS nanocrystals are over 40 nm across on average, and the size distribution is broad (Table I). By using defocused imaging conditions, central light-contrast features became visible in some of the CdS nanoparticles (not shown).

PbS nanocrystals formed by ion implantation into α–Al_2O_3 have the cubic rock salt structure and exhibit a strong tendency to form a nearly continuous layer parallel to the specimen surface [Fig. 9(c)]. The individual PbS precipitates that did not form a continuous layer are also generally elongated parallel to the specimen surface. Most of the precipitates are oriented with their *c*-axis parallel to that of the host Al_2O_3, but a minor component of the PbS is aligned with its [111] axis parallel to the [0001] axis of the α-alumina.

C. Sulfide nanocrystals in Si

Sulfide nanoparticles formed by ion implantation into a silicon host are morphologically distinct from those formed in SiO_2 glass or in crystalline Al_2O_3. In the case of ZnS, the nanoparticles are faceted, have the cubic zincblende structure, and are aligned cube-on-cube with the silicon host [Fig. 10(a)]. Most of the largest ZnS precipitates are located at a depth of 300–400 nm—just behind the region of maximum irradiation damage. In previous work, we showed that ion irradiation at low temperature could be used to amorphize the silicon while leaving the ZnS precipitates in a crystalline and coher-

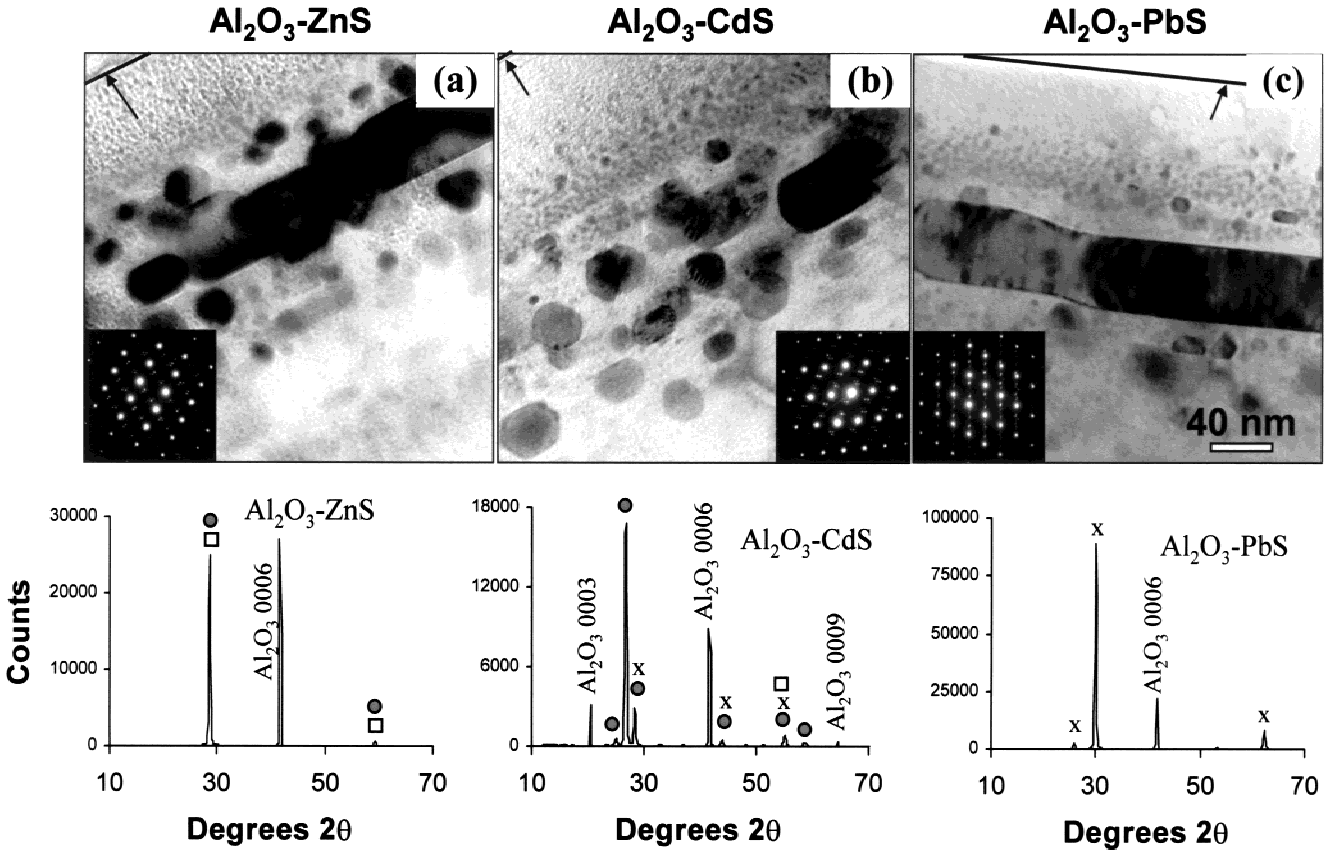

FIG. 9. (a–c) Sulfide precipitates in α–Al_2O_3. The implantation and annealing conditions are given in Table I. The x-ray diffraction results for each specimen are shown below the corresponding TEM micrograph. The peak positions for the wurtzite structure are marked by a circle, those for the zincblende structure are marked by a square, and those for the rock salt structure are marked by an x. Arrows point to the specimen surface.

ently aligned state.[26] If the radiation resistance of the precipitate and host compositions are different, unique microstructures of this type can easily be formed.

The CdS precipitates in silicon are also well-faceted and aligned cube-on-cube with the silicon host. The (111) facets (with respect to the host silicon) are particularly well developed, and the precipitates appear diamond-shaped in the [011] zone-axis image [Fig. 10(b)]. The shape of the nanocrystals is not necessarily the equilibrium shape for CdS but instead reflects the opening of the silicon lattice to accommodate the precipitate. Images taken at higher magnifications showed bent or curved moiré fringes, suggesting a significant amount of strain within the CdS nanocrystals. Despite the lower ion dose, relatively more particles appear to have crystallized than for the case of ZnS.

In contrast to the cases for ZnS and CdS, PbS precipitates did not form after implantation of Pb and S followed by thermal processing. Instead, the only peaks observed in a θ–2θ scan (apart from those of the host Si) were indexable to metallic Pb. Similarly well-aligned Pb precipitates were previously reported to form after Pb implantation into crystalline Si at 650 °C.[27]

IV. DISCUSSION

For potential applications in optoelectronic devices, the desired attributes of nanoparticle/host systems are that the host should be transparent and durable, the host material should contain a high volume-filling fraction of nanoparticles, and the nanocrystals should have narrow size distributions and simple microstructures. As shown in Figs. 1 to 10, the first two requirements can be met by the ion-implantation technique, however, the third requirement is generally not satisfied. To investigate possible means by which narrow size distributions and simple microstructures can be obtained, the origin of some of these unusual microstructures is investigated.

A. Formation of undesirable phases

In general, the sulfides can be readily formed by ion implantation techniques. In fact, in these experiments, the only compound that did not form was PbS in a silicon host, where undesired metallic Pb particles formed rather than the PbS compound. The crystal structures of metallic Pb and PbS (space group *Fm3m* for both compounds) are relatively close to that of silicon (space group *Fd3m*).

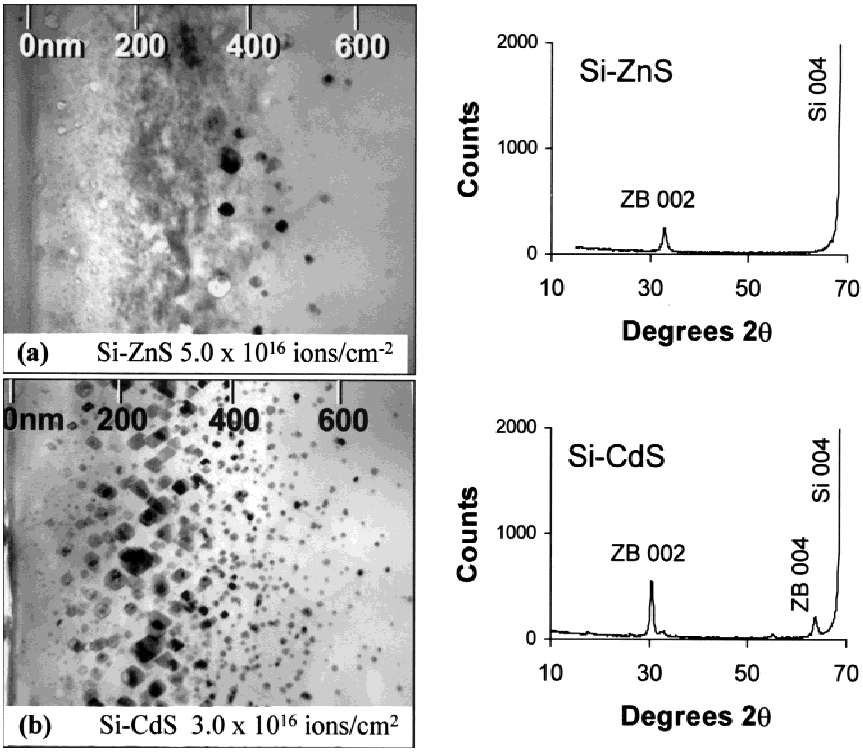

FIG. 10. (a,b) Sulfide precipitates in silicon. For each specimen, a cross-sectional micrograph is shown on the left, and the corresponding x-ray diffraction results are given on the right.

The lattice parameter of metallic Pb is smaller than that of Si by 9%, but that of PbS is larger by an equivalent 9%. The absolute difference between the lattice parameters of metallic Pb and Si (0.48 Å) is, however, smaller than that between PbS and Si (0.51 Å). Thus, there is no structural or crystallographic driving force to form PbS instead of Pb. On the other hand, zincblende ZnS and CdS have essentially the same cubic crystal structure and nearly the same lattice parameter as crystalline silicon, in contrast to metallic cadmium or zinc which are hexagonal (space group $P6_3/mmc$). Crystal structure and lattice matching are therefore key considerations in the formation of the desired nanocrystalline precipitates in crystalline hosts.

In the case of the Zn + S–implanted SiO_2 specimens, a Zn_2SiO_4 phase formed by reaction of the implanted zinc with the host SiO_2. This phase was also produced in SiO_2 specimens implanted with zinc only and annealed at high temperature (Fig. 2). In both cases, convergent beam or selected area electron-diffraction techniques were used to make this identification. The γ–Zn_2SiO_4 phase did not form before annealing the specimens and, in fact, γ–Zn_2SiO_4 is a rarely reported phase that was previously found to be a devitrification product in SiO_2:ZnO glass.[28] This phase apparently forms over a narrower compositional range than the more common α and β polymorphs of Zn_2SiO_4. Williamson and Glasser[28] reported that samples that were quenched in air from 1000 °C to room temperature showed numerous spherulites of γ–Zn_2SiO_4, and the cooling rate was found to be an important determinant for formation of this phase. Thus, a slower cooling rate or a lower annealing temperature could restrict the formation of the zinc silicate phase. Additionally, the electron-irradiation technique reported above could be used to grow ZnS precipitates without the cogenetic formation of zinc silicate.

B. Bimodal size distributions

Strongly bimodal size distributions were observed in all the annealed SiO_2–ZnS specimens except for SiO_2–ZnS–1 (low ion dose). In the specimens implanted with a single ion energy, the layer of large precipitates is located at a depth of about 300 nm. Figure 11 shows the results of a TRIM calculation (full damage cascades) for the implant conditions corresponding to specimens SiO_2–ZnS–4,5, and 6 (i.e., 320 keV Zn^+ + 180 keV S^+). A value of 10 eV was used for the atomic displacement energy of SiO_2.[29] The distribution of irradiation-produced vacancies is shown for each ion in Fig. 11, as well as the calculated median range of the implanted ions (i.e., the depth for the maximum implanted concentration). The layer of large precipitates is located well beyond the median ion range and the depth for the peak ballistic damage. Based on the TRIM calculations, the actual number of atomic displacements in the SiO_2 glass at a depth of 300 nm is about 1.5 displacements per atom

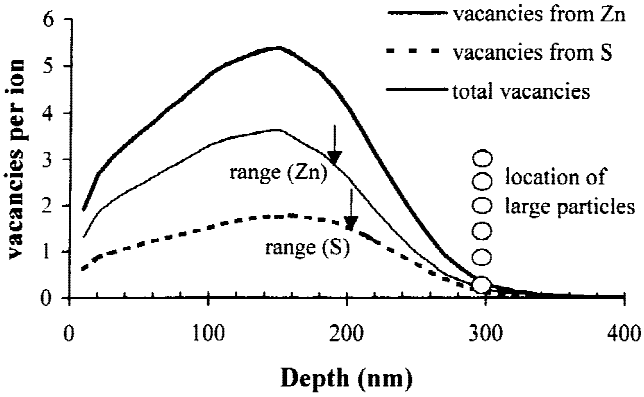

FIG. 11. Results of TRIM-96 calculations showing the distribution of ion irradiation damage, measured as the average number of vacancies per ion produced by zinc (thin line) and sulfur (dashed line) implantation into the SiO_2 host. Thick line represents the sum of the vacancies produced by both the implanted Zn and S. Ion energies corresponded to those used for the single-energy implants [see Table I and Fig. 1(d)–(f)]. The depth corresponding to the maximum concentration of the implanted ions is denoted by arrows, and the location of the layer of large precipitates [determined from Figs. 1(e) and 1(f)] is marked by circles.

(dpa). This value rapidly decreases to less than 0.1 dpa at a depth of about 330 nm. Crystalline quartz normally amorphizes at 0.2 dpa in the temperature range relevant to these experiments.[30] Assuming that this dpa level is the same as that required to transform the SiO_2 structure from that of normal SiO_2 glass to ion-beam-amorphized SiO_2 (the two structures are clearly different[31]), then the location of the layer of larger precipitates corresponds closely to the calculated boundary between the radiation-damaged SiO_2 and the undamaged glass at deeper levels.

Bonafos *et al.*[19] previously reported the self-organization of ZnS nanocrystals produced by ion implantation in fused silica; however, two bands of larger precipitates were observed that corresponded closely to the regions of maximum ion damage for the Zn and S implants. In contrast, in these experiments, the band of large precipitates was observed near the maximum *depth* of the irradiation damage in the SiO_2 host. Bonafos *et al.*[19] did not attempt to overlap the Zn and S concentrations (both ions were implanted at the same energy), and they tentatively attributed the formation of this banded structure to a quasi-Ostwald ripening self-organization effect, as predicted by computer simulations.[32,33]

The results shown in Fig. 2 demonstrate that the size layering effect observed in the SiO_2–ZnS specimens is attributable to the behavior of the implanted zinc and not to that of the sulfur. In addition to reacting with the host SiO_2, the Zn apparently has a strong tendency to move to the maximum depth of the ion-irradiation damage in the host silica glass. The reason for this behavior is not known, but one possibility is that the diffusion of Zn may be slower in the nonirradiated glass than in the radiation-damaged material. The concept of enhanced diffusion effects in radiation-damaged SiO_2 glass is consistent with the previous observation of the depth distribution of Ag and Cu in implanted soda lime glass.[34] When the glass was preimplanted with 200 keV Ar ions, the distribution of Ag and Cu extended considerably further into the specimen. Analysis of Fig. 7 in Ref. 34 indicates that, in fact, the implanted copper may have diffused to near the calculated end-of-range of the Ar ions (based on TRIM-96 calculations). The ultimate distribution of some implanted elements (e.g., Zn in this work) is therefore strongly affected by radiation-induced structural modifications in the host glass.

Several other variables appear to influence the size layering effect in the SiO_2–ZnS and SiO_2–Zn specimens shown in Figs. 1 and 2. When sulfur is implanted first, the zinc concentration profile does not extend as far into the specimen (e.g., compare samples SiO_2–ZnS–2 and SiO_2–ZnS–3 in Fig. 1). This suggests that the initial implantation of sulfur in some way restricts the thermal diffusion of both species to the interface between the ion-irradiated glass and the undamaged glass at deeper levels. In the specimen implanted with Zn only, a layer of large precipitates occurred at a depth of about 250 nm, but an additional layer of larger particles formed at a depth of about 110 nm (Fig. 2). In addition to the effects of radiation damage described above, chemical effects (e.g., the reaction of zinc and sulfur to form ZnS, as well as the formation of Zn_2SiO_4 by reaction with the host) play an important role in the ultimate distribution of the nanocrystals.

In the case of ZnS in silica glass, we were not able to eliminate the bimodal size distribution by changing the annealing time (6 to 60 min) or the annealing atmosphere (neutral or reducing). In further experiments, we have recently found that the size banding effect does not occur after thermal processing at 600 °C. Other low-temperature means of forming ZnS particles are therefore clearly needed. Accordingly, the initial electron-irradiation results presented in Sec. III. 2 are significant, and further irradiation-induced nucleation experiments are currently under way.

C. Central voids in CdS nanocrystals

Two potential mechanisms are considered that could account for the large central voids observed in the CdS precipitates. First, void formation may occur in a crystalline lattice owing to vacancy aggregation during irradiation (e.g., see Refs. 35–37). This process usually leads to a layer of small (~3 nm) voids in the near-surface region of irradiated alumina,[38] consistent with the near-surface voids visible in the ion-implanted alumina specimens in these experiments (Fig. 9). A similar effect has not been reported in ion-irradiated SiO_2 glass[39] (e.g., see Fig. 1). Alternatively, the implantation of a gaseous species (e.g., H or He) followed by thermal processing can

produce relatively large, faceted voids in crystalline silicon.[40–43] These voids have been suggested to form as a result of accumulation of the implanted gas at irradiation-produced defects in the host material. Such cavities can grow to be relatively large (>10 nm in diameter).[41]

To further examine these two mechanisms, two additional SiO_2–CdS specimens were prepared. One sample was implanted at room temperature, but in this case, the sample was heat sunk during implantation to reduce ion-beam heating. The other specimen was implanted at 500 °C. The implanted ion dose was 7.5×10^{16} ions/cm^2 for each constituent, and the specimens were annealed at 1000 °C for 1 h in Ar + 4%H_2.

If the voids form by vacancy coalescence, then the implantation temperature may play a role. More vacancies are expected to survive during irradiation at low temperatures; however, vacancy clustering depends on the temperature at which the vacancies become mobile. Conversely, the implanted sulfur could behave like an implanted gas either during implantation or during thermal processing, thereby creating voids in a process analogous to that described for crystalline silicon.[41] The temperature of the non-heat-sunk specimens during implantation was estimated by the method described in Ref. 44 to be at least 200 °C. The vapor pressure of sulfur is orders of magnitude higher than that of the transition metals at temperatures above 200 °C.

Hollow nanocrystals of CdS did not occur in the heat sunk specimen (Fig. 12), even though the thermal processing was the same as for the other samples (this experiment also rules out the possibility of the voids forming during TEM specimen preparation). Many of the CdS nanocrystals were strongly twinned [Fig. 12(b)]. On the other hand, numerous hollow particles occurred in the specimen implanted at 500 °C. Thus, there is a strong temperature effect in the formation of the voids: at low implant temperature voids are not produced, but at a high implant temperature they are numerous.

Vacancy clustering, in our opinion, is not likely to be the sole source of the central voids. The voids are large compared with vacancy voids produced by irradiation of crystalline host materials (e.g., Al_2O_3)[38]. Additionally, vacancy clustering does not explain why voids are generally not found in single-component nanocrystals produced by ion implantation (e.g., see Refs. 45–47). Vacancy clustering probably does play a minor role (e.g., to produce void embryos within the precipitates to which an implanted gas may diffuse and aggregate to produce the larger voids observable in Fig. 5). Particle size (or implant concentration) also appears to be important, because only the larger nanocrystals, located near the maximum implanted concentration in the highest-dose sample, appear to contain voids.

D. Controlling size distributions

The size distributions observed for compound nanocrystals produced by ion implantation are generally large, but of the various experimental parameters investigated here, four stand out as important means of reducing the size dispersion: the use of an amorphous as opposed to a crystalline host, the total implanted ion concentration, the use of multienergy implants to form a relatively flat concentration profile of the implanted species, and the use of nonthermal techniques to nucleate and grow the nanocrystal precipitates.

Reducing the ion dose has the effect of narrowing the size distribution and results in smaller nanocrystals (Table I, Fig. 13) for the experimental conditions investigated here. This observation is essentially a result of the presence of small particles in the tails of the implant distribution that occurred even for the highest-dose samples. Longer annealing times could potentially reduce the concentration of these smaller particles due to Ostwald ripening and growth of the larger precipitates. Multiple energy implants can assist this process by providing a constant concentration of the implanted species.

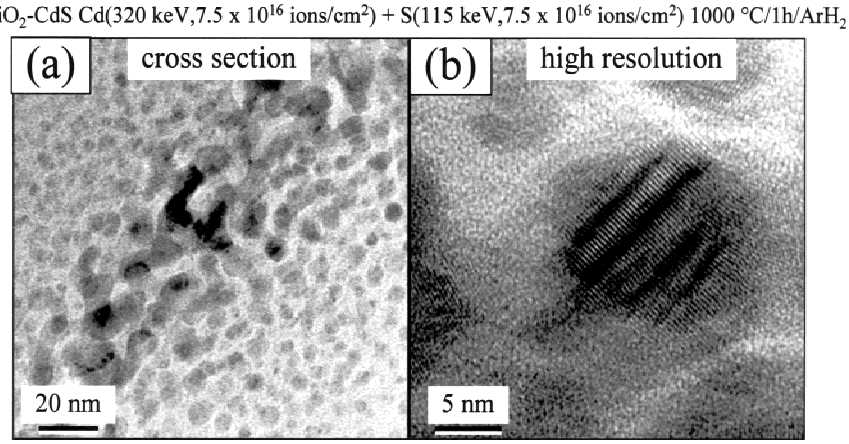

FIG. 12. (a,b) CdS precipitates in silica glass. The specimen was heat sunk during implantation. Hollow particles are not present.

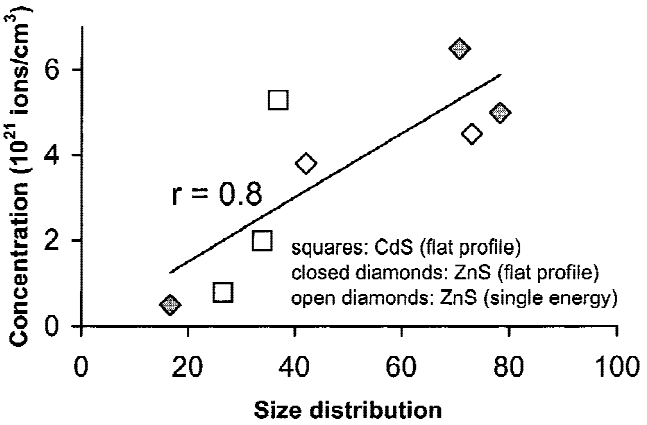

FIG. 13. Relative width of the size distribution for the SiO_2–ZnS and SiO_2–CdS specimens as a function of the implanted concentration as measured by RBS analysis. The width of the size distribution is given by the formula: $W = 100 \times$ (standard deviation) $\div$ (average diameter). With increasing implanted concentration, the size distribution becomes correspondingly wider (correlation coefficient, $r = 0.8$). Multienergy implants (flat profile) gave slightly narrower size distributions.

For example, the multienergy, low-dose ZnS implants into SiO_2 glass give a relatively narrow size distribution, and the formation of the large nanocrystals at the end of range is almost entirely suppressed. These general rules appear to apply equally well for CdS nanocrystals in SiO_2: the narrowest size distribution was achieved for the low-dose, multienergy specimen. For additional single-energy implants used to form CdS, the concentration gradient near the surface resulted in a widening of the size distribution, and at high doses the size distribution also increased (although not as much as for the case of ZnS) and relatively large voids were observed. Similarly, for PbS, decreasing the dose narrowed the size distribution. Multienergy low-dose implants were not done for PbS in SiO_2but we anticipate that the resulting size distribution would be narrower than that obtained for the single-energy implant reported here.

Implanting into a crystalline substrate instead of silica glass has the effect of producing larger nanocrystals at a similar ion dose. The nanocrystals are faceted and three-dimensionally aligned with the matrix. The structure and orientation of the nanocrystals can be controlled by the selection of the host material (e.g., compare Figs. 9 and 10). However, even at the lowest dose investigated (4×10^{16} ions/cm^2 for PbS in Al_2O_3), the size distribution was quite large. Apparently, nucleation is suppressed in these crystalline substrates so that fewer, but larger, nanocrystals are formed. Thus, if the size distribution is critical, then a noncrystalline host material provides better results.

V. CONCLUSIONS

The microstructure and size distributions of sulfide nanocrystals produced by ion-implantation techniques were investigated by cross-sectional TEM techniques. Several unusual or unexpected features were observed, including:

(1) Strongly bimodal size distributions, particularly for ZnS nanocrystals in silica glass. A layer of large ZnS precipitates forms at the maximum depth of the irradiation damage.

(2) The formation of a new phase, γ-Zn_2SiO_4, in SiO_2 glass implanted with Zn + S and with Zn only. This phase occurred as polycrystalline spherulitic aggregates.

(3) Central light-contrast features in the CdS nanocrystals. EELS analysis confirmed that these features were voids or bubbles.

(4) The formation of continuous layers of the sulfides in Al_2O_3. This layering effect did not occur in the silicon host. The structure and orientation of the precipitates could be controlled by the choice of crystalline host material.

These experiments demonstrate means by which narrower size distributions can be obtained for sulfide nanocrystals formed by ion implantation. The most important parameters were found to be the implant dose, the structure of the host (i.e., crystalline or amorphous), and the annealing temperature. Specimens implanted with several ion energies to give a nearly flat concentration profile demonstrated somewhat narrower size distributions. Initial results suggest that nonthermal nucleation of sulfide nanocrystals may produce significantly better results in terms of the size distribution and microstructural complexity. Further experiments are under way to investigate the irradiation-induced nucleation and growth of compound semiconductor nanocrystals.

ACKNOWLEDGMENTS

A.M. acknowledges support from the Natural Sciences and Engineering Research Council of Canada. Oak Ridge National Laboratory is managed by Lockheed Martin Energy Research Corp. for the United States Department of Energy under Contract No. DE-AC05-96OR22464. The microscopy was performed in part at the SHaRE User Facility, which is supported by the Division of Materials Sciences, United States Department of Energy.

REFERENCES

1. A.P. Alivisatos, Science **271,** 933 (1996).
2. A.N. Goldstein, C.M. Echer, and A.P. Alivisatos, Science **256,** 1425 (1992).
3. S. A. Empedocles, D. J. Norris, and M. G. Bawendi, Phys. Rev. Lett. **77,** 3873 (1996).
4. G. Allan, C. Delerue, and M. Lannoo, Phys. Rev. Lett. **76,** 2961 (1996).
5. T.D. Krauss and F.W. Wise, Phys. Rev. B **55,** 9860 (1997).
6. V. Sukumar and R.H. Doremus, Phys. Stat. Sol. B **179,** 307 (1993).
7. M. Tan, W. Cai, and L. Zhang, Appl. Phys. Lett. **71,** 3697 (1997).
8. J. Tittel, W. Göhde, F. Koberling, Th. Basche, A. Kornowski, H. Weller, and A. Eychmüller, Phys. Chem. B **101,** 3013 (1997).

9. P.D. Persans, H. Yükselici, L.B. Lurio, J. Pant, M. Stapleton, and T.M. Hayes, J. Non-Cryst. Sol. **203,** 192 (1996).
10. R.N. Barghava, D. Gallagher, X. Hong, and N. Nurmikko, Phys. Rev. Lett. **72,** 416 (1994).
11. G. Gallagher, W.E. Heady, J.M. Racz, and R.N. Barghava, J. Mater. Res. **10,** 870 (1995).
12. Y. Yang, J. Huang, S. Liu, and J. Shen, J. Mater. Chem. **7,** 131 (1997).
13. S.A. Gurevich, A.I. Ekimov, I.A. Kudryavtsev, A.V. Osinskii, V.I. Skopina, and D.I. Chepik, Sov. Phys. Semicond. **26,** 57 (1992).
14. C.W. White, J.D. Budai, S.P. Withrow, J.G. Zhu, E. Sonder, R.A. Zuhr, A. Meldrum, D.M. Hembree, D.O. Henderson, and S. Prawer, Nucl. Instr. Meth. Phys. Res. **B141,** 228 (1998).
15. M.G. Bawendi, P.J. Carroll, W.L. Wilson, and L.E. Brus, J. Chem. Phys. **96,** 946 (1992).
16. M.A. Hines and P. Guyot-Sionnest, J. Phys. Chem. **100,** 468 (1996).
17. A. Ekimov, S. Gurevich, I. Krudriavstev, O. Lublinskaya, A. Merkulov, A. Osinskii, M. Vatnik, M. Gandais, and Y. Wang, J. Cryst. Growth **151,** 38 (1995).
18. C.W. White, J.D. Budai, J.G. Zhu, S.P. Withrow, D.M. Hembree, D.O. Henderson, A. Ueda, Y.S. Tung, and R. Mu, in *Ion-Solid Interactions for Materials Modification and Processing*, edited by D.B. Poker, D. Ila, Y-T. Cheng, L.R. Harriott, and T.W. Sigmon (Mater. Res. Soc. Symp. Proc. **396,** Pittsburgh, PA, 1996), p. 377.
19. C. Bonafos, B. Garrido, M. López, A. Romano-Rodriguez, O. Gonzáles-Varona, A. Pérez-Rodriguez, and J.R. Morante, Appl. Phys. Lett. **72,** 3488 (1998).
20. J.D. Budai, C.W. White, S.P. Withrow, M.F. Chisholm, J.G. Zhu, and R.A. Zuhr, Nature **390,** 384 (1997).
21. J.G. Zhu, C.W. White, D.J. Wallis, J.D. Budai, and S.P. Withrow, in *Ion-Solid Interactions for Materials Modification and Processing*, edited by D.B. Poker, D. Ila, Y-T. Cheng, L.R. Harriott, and T.W. Sigmon (Mater. Res. Soc. Symp. Proc. **396,** Pittsburgh, PA, 1996), p. 447.
22. J.F. Ziegler, *Transport and Range of Ions in Matter*, Version 96.01 (IBM-Research, Yorktown, NY, 1996).
23. J.P. McCaffrey, B.T. Sullivan, J.W. Fraser, and D.L. Callahan, Micron **27,** 407 (1996).
24. C.B. Murray, C.R. Kagan, and M.G. Bawendi, Science **270,** 1335 (1995).
25. J.J. Shiang, A.V. Kadavanich, R.K. Grubbs, and A.P. Alivisatos, J. Phys. Chem. **99,** 17417 (1995).
26. A. Meldrum, R.A. Zuhr, E. Sonder, J.D. Budai, C.W. White, L.A. Boatner, R.C. Ewing, and D.O. Henderson, Appl. Phys. Lett. **74,** 697 (1999).
27. E. Johnson, A. Johansen, L. Sarholt, and U. Dahmen, Nucl. Instr. Meth. Phys. Res. **B148,** 1034 (1999).
28. J. Williamson and F.P. Glasser, Phys. Chem. Glasses **5**, 52 (1964).
29. H. Inui, H. Mori, T. Sakata, and H. Fujita, J. Non-Cryst. Sol. **116,** 1 (1990).
30. S.X. Wang, L.M. Wang, R.C. Ewing, and R.H. Doremus, J. Non-Cryst. Sol. **238,** 198 (1998).
31. L.C. Qin and L.W. Hobbs, J. Non-Cryst. Sol. **192&193,** 456 (1995).
32. V.A. Borodin, K-H. Heinig, and S. Reiss, Phys. Rev. B **56,** 5332 (1997).
33. S. Reiss and K.H. Heinig, Nucl. Instr. Meth. Phys. Res. B **84,** 229 (1994).
34. G.W. Arnold, P. Mazzoldi, L. Tramontin, A. Boscolo-Boscoletto, and G. Battaglin, in *Beam-Solid Interactions: Fundamentals and Applications*, edited by M. Nastasi, L.R. Harriott, N. Herbots, R. S. Averback (Mater. Res. Soc. Symp. Proc. **279,** Pittsburgh, PA, 1993), p. 285.
35. Y. Katano, K. Hojou, T. Nakazawa, T. Aruga, D. Yamaki, and K. Noda, Nucl. Instr. Meth. Phys. Res. **B141,** 411 (1997).
36. K. Gieselmann and D. Simon, J. Nucl. Mater. **203,** 83 (1993).
37. S.M. Murphy and A. Stokes, J. Nucl. Mater. **172,** 169 (1990).
38. E.D. Specht, D.A. Walko, and S.J. Zinkle, in *Crystallization and Related Phenomena in Amorphous Materials*, edited by M. Libera, T.E. Haynes, P. Cabe, and J.E. Dickenson, Jr. (Mater. Res. Soc. Symp. Proc. **321,** Pittsburgh, PA, 1994), p. 399.
39. W.J. Weber, R.C. Ewing, C.A. Angell, G.W. Arnold, A.N. Cormack, J.M. Delaye, D.L. Griscom, L.W. Hobbs, A. Navrotsky, D.L. Price, A.M. Stoneham, and M.C. Weinberg, J. Mater. Res. **12,** 1946 (1997).
40. J. Wong-Leung, J.S. Williams, R.G. Elliman, E. Nygren, D.J. Eaglesham, D.C. Jacobson, and J.M. Poate, Nucl. Instr. Meth. Phys. Res. **B96,** 253 (1995).
41. D.M. Follstaedt, S.M. Myers, G.A. Petersen, and J.W. Medernach, J. Electr. Mater. **25,** 151 (1996).
42. D.M. Follstaedt, Appl. Phys. Lett. **62,** 1116 (1993).
43. V. Raineri, P.G. Fallica, G. Percolla, A. Battaglia, M. Barbagallo, and S.U. Campisano, J. Appl. Phys. **78,** 3727 (1995).
44. J.A. Davies, W.N. Lennard, and I.V. Mitchell, in *Handbook of Modern Ion Beam Materials Analysis*, edited by J.R. Tesmer and M. Nastasi (Materials Research Society, Pittsburgh, PA, 1995), p. 343.
45. C.W. White, D.S. Zhou, R.A. Zuhr, and R.H. Magruder, in *Laser and Ion Beam Modification of Materials*, edited by I. Yamada, H. Ishiwara, E. Kamijo, T. Kawai, C.W. Allen, C.W. White (Trans. Mater. Res. Soc. Jpn. **17,** 1994) p. 553.
46. C.W. White, D.S. Zhou, J.D. Budai, R.A. Zuhr, R.H. Magruder, and D.H. Osborne, in *Materials Synthesis and Processing Using Ion Beams*, edited by R. Culbertson, O.W. Holland, K.S. Jones, and K. Maex (Mater. Res. Soc. Symp. Proc. **316,** Pittsburgh, PA, 1994) p. 499.
47. S. Honda, F.A. Modine, A. Meldrum, J.D. Budai, T.E. Haynes, L.A. Boatner, and L.A. Gea, in *Microstructural Processes in Irradiated Materials*, edited by S.J. Zinkle, G. Lucas, R.C. Ewing, and J. Williams (Mater. Res. Soc. Symp. Proc. **540,** Pittsburgh, PA, 1999), pp. 225–230.